IEEE Access
Multidisciplinary | Rapid Review | Open Access Journal

Received 19 March 2024, accepted 10 May 2024, date of publication 5 June 2024, date of current version 29 July 2024.

Digital Object Identifier 10.1109/ACCESS.2024.3409875

RESEARCH ARTICLE

Analysis of an Improved Circuit for Laser Chaos and Its Synchronization

ROBERTO CONCAS[1,2], ALESSIO MONTORI[2,4], EUGENIO PUGLIESE[5], ALESSIO PERINELLI[6,7], LEONARDO RICCI[6,7,8], (Member, IEEE), AND RICCARDO MEUCCI[3,5], (Senior Member, IEEE)

[1]Istituto Nazionale di Ricerca Metrologica (INRiM), 10135 Torino, Italy
[2]European Laboratory for Nonlinear Spectroscopy (LENS), 50019 Sesto Fiorentino, Italy
[3]Department of Physics, University of Florence (UNIFI), 50019 Sesto Fiorentino, Italy
[4]Istituto Nazionale di Ottica (CNR-INO), 50019 Sesto Fiorentino, Italy
[5]Istituto Nazionale di Ottica (CNR-INO), 50125 Firenze , Italy
[6]Department of Physics, University of Trento, 38123 Trento, Italy
[7]INFN-TIFPA, 38123 Trento, Italy
[8]CIMeC, Center for Mind/Brain Sciences, University of Trento, 38068 Rovereto, Italy

Corresponding author: Roberto Concas (r.concas@inrim.it)

This work was supported by Open Access Funding provided by Istituto Nazionale di Ricerca Metrologica within the CARE-CRUI Transformative Agreement.

ABSTRACT The exploration of chaos, synchronization, and circuit implementation in analog simulations unveils a versatile framework with diverse applications. Originating from a universal chaos model rooted in laser physics, its adaptability extends to neural dynamics and random number generation, where both rely on characteristic time scales. Circuit implementations using op-amps and analog multipliers offer tangible avenues for exploration. However, challenges like bias and trajectory distortion drive the need for innovative solutions. Through numerical integration and circuit simulations, analysis of chaotic regimes such as Sub-harmonic Chaos (SC) and Homoclinic Chaos (HC) reveals crucial behaviors for applications like secure communications. Despite experimental hurdles, advancements in circuit design promise novel pathways for chaos synchronization studies. Understanding the intricate interplay between chaos and these systems is vital, given their reliance on characteristic time scales. Additionally, exploring chaos synchronization, especially within analog circuits, shows potential for revolutionizing information processing capabilities, despite inherent challenges. Progress in circuit design persists, forging new avenues in chaos synchronization studies, shaping a dynamic landscape poised for further exploration and innovation.

INDEX TERMS Analog simulations, chaos, chaos synchronization, circuit design.

I. INTRODUCTION

The minimal universal model for chaos [1], [2], [3] has its origins in the physics of a laser subjected to a feedback that controls its losses via a simple low-pass filter with an appropriate cut-off frequency [4]. The feedback introduces a third degree of freedom, which is sufficient to produce self-pulsing and chaotic behavior when the feedback's cutoff frequency is comparable to the population inversion decay rate.

The associate editor coordinating the review of this manuscript and approving it for publication was Dušan Grujić.

However, the potential of this model is not limited to laser physics. This is because the relaxation rates of the three variables describing the system's evolution can be changed in very large intervals. For example, when dynamics occurs on time scales of the order of hundreds of milliseconds, the model shows interesting overlaps with the dynamics of neurons [5]. This is the case when a sub-threshold electrical activity of a neuron is interrupted by high amplitude pulses thus signaling action-potentials. Spiking activity is therefore a fundamental aspect of neuronal dynamics, reflecting a mechanism of accumulation and rapid energy release. Chaotic dynamics in phenomenological and

biologically inspired models of neurons have been explored in applications such as the analysis of epileptic seizures in EEG data [6], [7].

When the dynamics is driven to higher frequencies, the model was shown to be well-suited for applications in the field of random number generation [8], which is crucial for data transfer or storage and secure communications [9], [10].

The interest in this model also lies in applications related to its control when a small perturbation can change a chaotic state into a periodic one or vice versa [11] and synchronization when multiple systems are coupled.

For these applications, crucial issues are represented by a reliable analog implementation of a single dynamical system and coupling schemes for synchronization.

The paper is organized as follows: in Sec. II the circuit design is described, starting from the analysis of the differential equations underlying the model to the description of the proposed circuital implementation; in Sec. III the numerical and electronic simulations are presented along with the related analysis of the result in both the sub-harmonic bifurcation type regime and the homoclinic one; in Sec. IV the analysis of the synchronization between two independent circuits is discussed; in the concluding section we summarize and provide some outlook.

II. MINIMAL UNIVERSAL OSCILLATOR MODEL AND CIRCUIT DESIGN

A. MODEL EQUATIONS

The minimal universal laser model is described by the following system of first-order differential equations:

$$\frac{dx}{dt} = -k_0\,(x + k_1 x z^2 - xy), \tag{1a}$$

$$\frac{dy}{dt} = -\gamma\,(y + xy - p_0), \tag{1b}$$

$$\frac{dz}{dt} = -\beta\,(z - B_0 + B_1 x). \tag{1c}$$

In these equations: x is the "fast" variable that represents the laser output intensity and has a typical unperturbed decay rate $k_0 = 2 \cdot 10^7\ \mathrm{s}^{-1}$; y is the "slow" variable that represents the population inversion with pumping rate $\gamma\, p_0$ and has a typical decay rate $\gamma = 10^5\ \mathrm{s}^{-1}$; z is the "intermediate" feedback variable, which affects x in a nonlinear way (see the term xz^2 in the first equation) even if it is regulated in a linear way via a low-pass filter. This filter, characterized by a typical bandwidth $\beta = 10^6\ \mathrm{s}^{-1}$, is fed by the fast variable x, properly amplified by the factor B_1, along with a bias B_0.

It is interesting to note that the time evolution of the system can be modified without altering its dynamics, and thus the related phase portraits, by scaling the three rates k, γ, β by the same factor α: if the rates are divided by α, and $\alpha > 1$ ($\alpha < 1$), the dynamics is slowed (accelerated) by a factor α, as setting $\tau = \alpha t$ leaves Eqs. (1) unchanged.

In the following, this property was exploited to implement an electronic simulation of Eqs. (1) and thus to cope with the limited bandwidth response introduced by the analog electronic components: setting $\alpha = 10^3$, the typical values mentioned above for the three rates become

$$k_0' = \frac{k_0}{10^3} = 2 \cdot 10^4\ \mathrm{s}^{-1}, \tag{2a}$$

$$\gamma' = \frac{\gamma}{10^3} = 10^2\ \mathrm{s}^{-1}, \tag{2b}$$

$$\beta' = \frac{\beta}{10^3} = 10^3\ \mathrm{s}^{-1}, \tag{2c}$$

Consequently, the evolution becomes 10^3 times slower, as the system of equations gets

$$\frac{dx}{d\tau} = -k_0'\,(x + k_1 x z^2 - xy), \tag{3a}$$

$$\frac{dy}{d\tau} = -\gamma'\,(y + xy - p_0), \tag{3b}$$

$$\frac{dz}{d\tau} = -\beta'\,(z - B_0 + B_1 x), \tag{3c}$$

where

$$\tau = 10^3\, t\,. \tag{4}$$

B. CIRCUIT DESCRIPTION

The system of differential equations describing the minimal universal laser model can be solved via analog computation by using a suitable combination of integrated circuits, namely op-amps and analog multipliers, and passive electronic components.

As mentioned in the Introduction, the implementation proposed by Ricci et al. [2] is affected by issues leading to the presence of an undesired bias term and the unwanted distortion of the trajectory in phase space. The circuit proposed here provides an elegant and effective solution to these problems. The design block shown in Fig. 1 relies

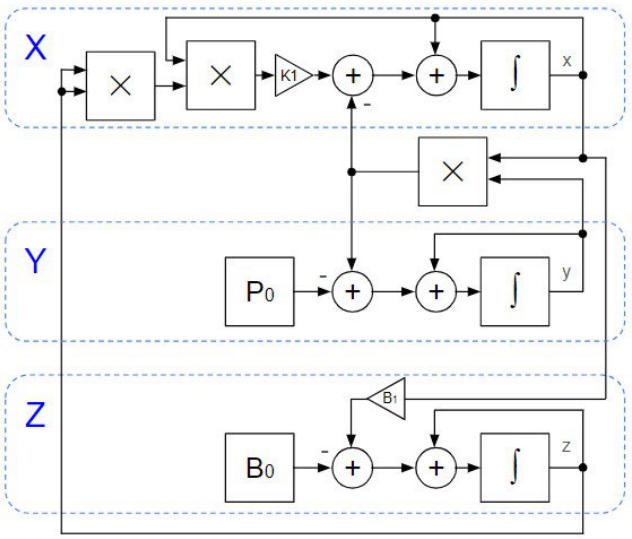

FIGURE 1. Design block of the implementation of the minimal universal model. The architecture consists of three functional blocks *X*, *Y*, *Z*, each enclosed by a blue, dashed line, that implement the differential equations providing *x*, *y*, *z*.

on three multipliers and three summing integrators, which produce the outputs x, y, z and are characterized by the time constant τ_X, τ_Y, τ_Z, respectively. The circuit implementation of this architecture is shown in Fig. 2. All active components are assumed to be power supplied with ± 15 V.

The nonlinear terms are obtained by using three identical blocks, each containing an analog multiplier AD633JN and a noninverting amplifier based on the operational amplifier (op-amp) AD820. Given the five multiplier inputs $\hat{X}$, $\hat{X}_0$, $\hat{Y}$, $\hat{Y}_0$, $\hat{Z}_0$, the output $\hat{W}$ of the analog multiplier AD633JN is given by

$$\hat{W} = \frac{1}{V_0}(\hat{X} - \hat{X}_0)(\hat{Y} - \hat{Y}_0) + \hat{Z}_0\,, \tag{5}$$

where $V_0 = 10$ V.
In the present implementation, $\hat{X}_0 = \hat{Y}_0 = \hat{Z}_0 = 0$. The output $\hat{W}$ is then amplified by a factor 10 due to $R_i = 1\,\text{k}\Omega$, $R_f = 9\,\text{k}\Omega$. Consequently, given the inputs A, B, each nonlinear block generates an output C given by

$$C = \frac{A \cdot B}{1\,\text{V}}\,. \tag{6}$$

The integrator producing y is based on the op-amp AD820 and is fed with the terms V_1, xy, y. (The one producing x is described below.) By using a standard analysis in the Laplace frequency domain the output of the op-amp is given by

$$-\frac{s}{\gamma'}\,\tilde{y} = \tilde{y} + \frac{R_6}{R_5}\,\widetilde{xy} - p_0 \tag{7}$$

where $s = j\omega$, $\tilde{A}$ represent the Laplace transforms of a generic time-dependent quantity A, and

$$\gamma' = (R_6 C_2)^{-1}\,. \tag{8a}$$

$$p_0 = -\frac{R_6}{R_7} V_1\,. \tag{8b}$$

By setting

$$R_5 = R_6\,, \tag{9}$$

the block producing y turns out to implement Eq. (3b).

The integrator producing z is based on the op-amp AD820 and is fed with the terms V_2, x and z. In the frequency domain, we have

$$-\frac{s}{\beta'}\,\tilde{z} = \tilde{z} - B_0 + B_1\,\tilde{x} \tag{10}$$

where

$$\beta' = (R_9 C_3)^{-1}\,. \tag{11a}$$

$$B_1 = \frac{R_9}{R_8}\,, \tag{11b}$$

$$B_0 = -\frac{R_9}{R_{10}}\,V_2\,. \tag{11c}$$

In this way the block producing z turns out to implement Eq. (3c) directly.

The integrator producing x is based on the op-amp AD8676 and is fed with the terms xz^2, xy, x. In the frequency domain, we have

$$-\frac{s}{k_0'}\,\tilde{x} = \tilde{x} + k_1'\,\widetilde{xz^2} - k_2(s)\,\tilde{xy} \tag{12}$$

and

$$k_0' = (R_1 C_1)^{-1}\,, \tag{13a}$$

$$k_1' = \frac{R_1}{R_2}\,. \tag{13b}$$

The introduced factor $k_2(s)$ is defined as:

$$k_2(s) = \frac{R_4}{R_2}\,\frac{R_1 + R_2(1 + sR_1C_1)}{R_4 + R_3(1 + sR_4C_4)} \tag{14}$$

It is straightforward to show that $k_2(s) = 1$ independently of s if

$$\frac{R_3}{R_4} = \frac{R_1}{R_2}\,, \tag{15a}$$

$$C_4 = C_1\frac{R_1}{R_3}\,. \tag{15b}$$

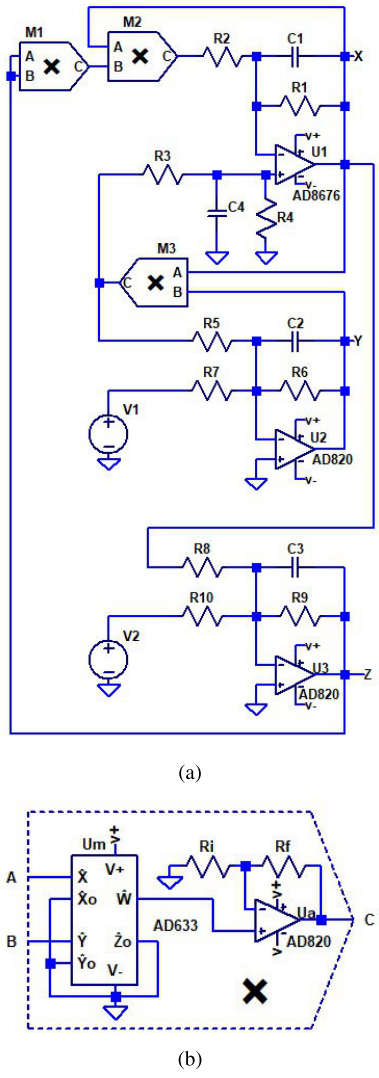

FIGURE 2. (a) Schematic of the circuit implementing the minimal universal model. (b) Structure of a single nonlinear block, having two input ports *A*, *B* and an output port *C*.

Consequently, by complying with these two conditions, the block producing x turns out to implement Eq. (3a), as it can be promptly verified by inverting the previous equation in the frequency domain s.

The chosen implementation of the differential equation for x shows different advantages compared with previous solutions [1], [2]. First, the contribution xy being fed into the noninverting input of U_1 via a carefully trimmed network (see Eq. (15b) above), allows to save an op-amp to generate the sign inversion of xy. However, the possibly most important improvement consists in the suppression of bias effects that, for example, had to be compensated for in the implementation discussed by Ricci et al. [2] via a manual adjustment of two trimmers.

III. SIMULATION AND ANALYSIS OF CHAOS

The analysis of the proposed design is carried out with two different approaches: numerical integration and circuit simulation. The results of the comparison between the numerical integration of the model described by Eqs. (1), the circuit simulation based on the electronic scheme of Fig. 2 and described by Eqs.(3) is summarised in Fig. 3.

As mentioned above, two chaotic regimes are considered. The first one, referred to as Sub-harmonic Chaos (SC), is a chaotic regime obtained after sub-harmonic bifurcations of a limit cycle originated from a Hopf bifurcation. The second regime is named Homoclinic Chaos (HC) and is characterised by pulses of the same height but erratically separated in time due to the re-injection mechanism around the local chaos SC. The re-injection mechanism is provided by the stationary solution of Eqs. (1) with zero intensity.

A. NUMERICAL INTEGRATION

A numerical integration of Eqs (1) was performed by using Berkeley Madonna software and relying on the built-in Runge-Kutta 4th order integrator with an integration step of 0.1 μs. The fixed parameter values are:

$$k_0 = 2\cdot 10^7\,\mathrm{s}^{-1}\,,\ \gamma = 10^5\,\mathrm{s}^{-1}\,,\ \beta = 10^6\,\mathrm{s}^{-1}\,,$$
$$k_1 = 33\,,\ B_1 = 0.222\,,\ p_0 = 1.4\,. \tag{16}$$

The two chaotic regimes are obtained by setting the adjustable parameter B_0 as follows:

$$B_0 = \begin{cases} 0.0938, & \text{for SC.} \\ 0.0941, & \text{for HC.} \end{cases} \tag{17}$$

The resulting phase portraits in the $x-z$ space and the related x time series are shown in Figs. 3a, 3b, 3e, 3f.

B. SPICE SIMULATION

The analog electronic simulation was carried out by using the software spice-based LTSpice®, which allows to reliably simulate analog or digital electronic circuits by means of models of electronic components used therein. This type of electronic simulation can consider nonidealities and limits of the components and it reproduces the full electronic behavior of op-amps and multipliers such as output voltage dynamic, input offset voltage, slew rate, multiplier's non-linearity. Consequently, simulations mostly faithfully reproduce what would result from real implementations.

Considering the design of Fig. 2, embedded spice models were used for both the passive components and the op-amps, whereas a basic spice model for multipliers was chosen. Once the boundary conditions are assigned, and neglecting a transient of 0.5 s, the simulation covers a span of 5 s.

The chosen nominal values of the passive components are listed in Table (1).

TABLE 1. Nominal values set for the passive components.

Component	Value
R_1	33 kΩ
R_2	1 kΩ
R_3	330 kΩ
R_4	10 kΩ
R_5	10 kΩ
R_6	10 kΩ
R_7	10 kΩ
R_8	4.5 kΩ
R_9	1 kΩ
R_{10}	1 kΩ
C_1	1.5 nF
C_2	1 μF
C_3	1 μF
C_4	150 pF

The choice complies with the constraints set by Eqs. (15a), (15b), (9).

According to Eqs. (13a), (8a), (11a), the resulting time constants are:

$$k_0' = 2.02\cdot 10^4\,\mathrm{s}^{-1}\,,\quad \gamma' = 10^2\,\mathrm{s}^{-1}\,,\quad \beta' = 10^3\,\mathrm{s}^{-1}\,. \tag{18}$$

Similarly, according to Eqs. (13b), (11b), the parameters k_1, B_1 are given by

$$k_1 = 33\,,\quad B_1 = 0.222\,, \tag{19}$$

whereas, according to Eqs. (8b), (11c), the parameters p_0, B_0 are given by

$$p_0 = -V_1(\mathrm{V})\,,\quad B_0 = -V_2(\mathrm{V})\,. \tag{20}$$

Finally, the tunable voltage parameters are

$$V_1 = -1.4\,\mathrm{V} \quad\Rightarrow\quad p_0 = 1.4\,, \tag{21}$$

and the two chaotic regimes are obtained by setting

$$V_2 \begin{cases} -0.0946\,\mathrm{V} & \Rightarrow \quad B_0 = 0.0946, \text{ for SC.} \\ -0.0956\,\mathrm{V} & \Rightarrow \quad B_0 = 0.0956, \text{ for HC.} \end{cases} \tag{22}$$

The results of the electronic simulation results are displayed in Figs. 3c, 3d, 3e, 3h.

Figures 3 point at a remarkable similarity between the numerical integration and the spice simulation results. Figure 3d highlights the predicted advantage of the architecture when HC is considered: the slightly squared-off trajectory for the variable x it is no more present as in

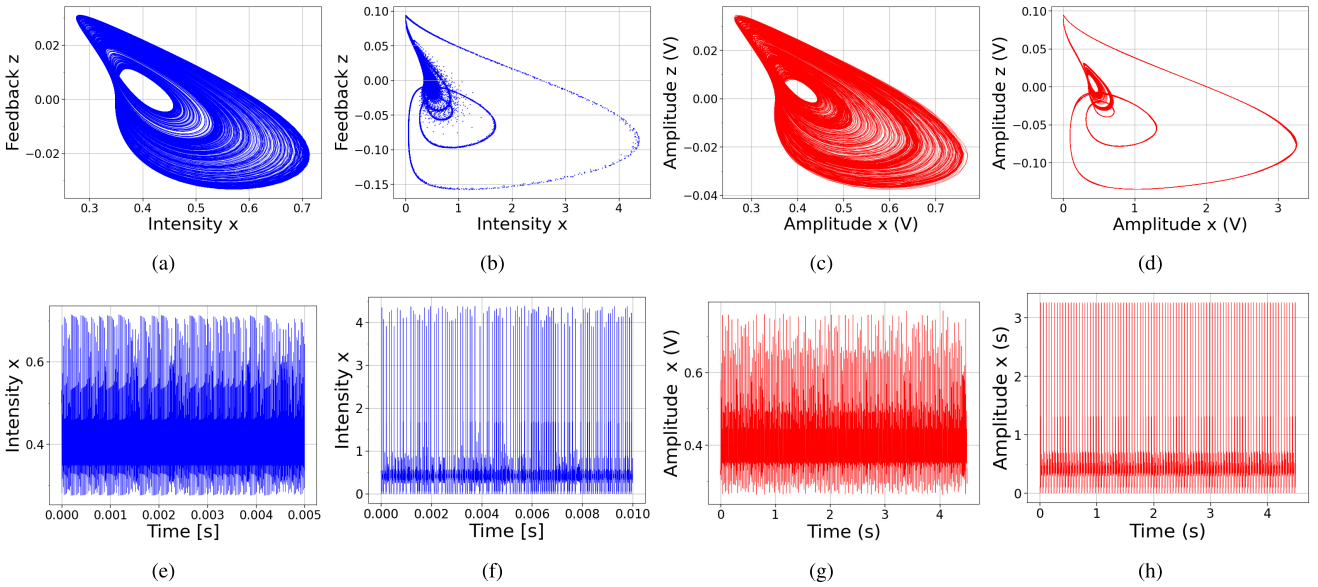

FIGURE 3. Numerical integration of Eqs.(1) (blue panels): (a) SC attractor in phase space *x*-*z*; (b) HC attractor in phase space *x*-*z*; (e) SC time series of the variable *x*; (f) HC time series of the variable *x*; Spice simulation of Eqs.(3) (red panels): (c) SC attractor in phase space *x*-*z*; (d) HC attractor in phase space *x*-*z*; (g) SC time series of the variable *x*; (h) HC time series of the variable *x*.

previous implementations [1], [2]. Due to the presence of the additional amplification following the multipliers (see Fig. 2), the dynamics is kept within the output voltage swing of the op-amps and consequently it prevents the saturation for the output voltages close to the power supply voltage.

C. EVIDENCE OF A CHAOTIC BEHAVIOR

An interesting point concerns the evidence of a chaotic behavior hinted at by the shape of the attractors shown in Fig. 3. Finding the evidence of chaos is a nontrivial task, especially when one has to rely on scalar time series. Although chaos can be shown to exist by knowing the nonlinear differential equations underlying a system and thereupon evaluating the Lyapunov spectrum via the so-called standard method [12], [13], in compliance with the approach followed in the present work, here we carried out an analysis on the time series stemming from the numerical simulations.

To look for chaos, we followed an approach [14] that relies on: first, the assessment of the correlation dimension on a "lattice" [15] of embedding pairs (m, L), where m, L are the dimension and the lag of the embedding, respectively; second, the identification of a hyperbolae-bounded region in which the correlation dimension is essentially constant and larger than 2; the evaluation of the maximum Lyapunov exponent (MLE) by using the "divergence rate method" [16], [17].

The "chasing chaos" protocol outlined above was carried out on a time series made of $2.5 \cdot 10^5$ points corresponding to the variable X and resulting from the numerical integration described in Sec. III-A. The correlation dimension was evaluated by using a recently-developed method [18] on a lattice of 380 embedding (m, L) points, where $2 \leqslant m \leqslant 20$, $1 \leqslant L \leqslant 20$. The diagram in Fig. 4 (a) shows the results of the evaluation. Figure 4 (b) shows the plot of the evaluated correlation dimension $\hat{\nu}$ as a function of the embedding window $(m-1)L$. A horizontal straight line fit to the 15 black points within the interval $110 \geqslant (m-1)L \geqslant 200$ provides $\hat{\nu} = 2.25 \pm 0.01$ and a reduced χ^2 of 0.86.

The embedding pairs belonging to the uniformity region for the correlation dimension are expected to provide reliable embedding choices for the evaluation of the MLE too [14], [17]. As mentioned above, this evaluation was carried out by means of the divergence rate method. The results are shown in Fig. 5: the estimated MLE is $(23 \pm 1)\,\mathrm{ms}^{-1}$.

IV. SYNCHRONIZATION BETWEEN CIRCUITS

synchronization of chaotic behavior in coupled lasers has become a hot issue since the seminal paper on chaos synchronization by Pecora and Carroll in 1990 [19].

synchronization emerges as a consequence of the addition of a forcing term to the systems or by suitably coupling them [20]. The emergence of synchronization phenomena is interesting for information processing processes, in order to achieve high-rate and secure communications [21], [22]. More recently, synchronization in a network of dynamical systems where the connected oscillators become transceiver nodes was investigated [23].

Chaos synchronization between two lasers has been experimentally confirmed in solid state lasers [24], CO_2 lasers [25], and semiconductor lasers [26], [27]. synchronization of globally coupled identical modulated laser models via the linear and nonlinear forms of diffusive couplings was also recently investigated [28].

synchronization between two circuits of the kind discussed by Ricci et al. [2] failed to be experimentally observed,

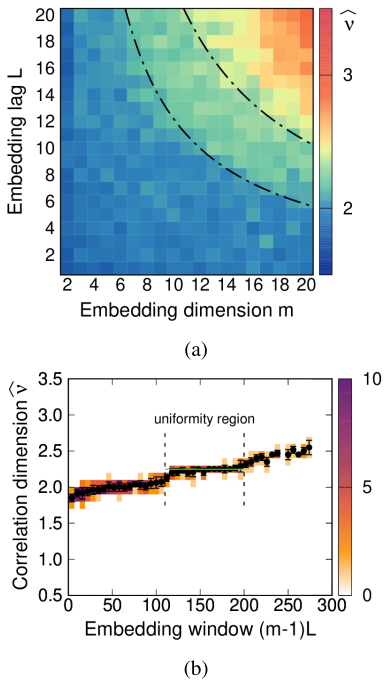

FIGURE 4. (a) Color map of the estimated correlation dimension $\hat{\nu}$ on the embedding lattice $2 \leqslant m \leqslant 20$, $1 \leqslant L \leqslant 20$. The dash-dotted lines represent the two hyperbolae $(m-1)L = 110$, $(m-1)L = 200$ that bound the uniformity region. (b) Estimated correlation dimension $\hat{\nu}$ as a function of the embedding windows $(m-1)L$. The color map represents the joint histogram of $\hat{\nu}$, $(m-1)L$, built with a bin size of 0.1 and 6, respectively. The black dots and errorbars correspond to the average and standard deviation, respectively, of each marginal histogram at a given embedding window. The uniformity region highlighted in (a) corresponds to the embedding-window-independent behavior of $\hat{\nu}$ between the embedding window values 110, 200. The green segment corresponds to the best-fit horizontal straight line at $\hat{\nu} = 2.25$.

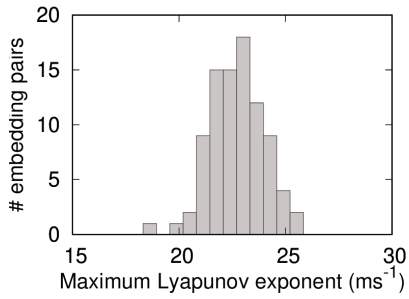

FIGURE 5. Histogram of the MLE computed on the embedding pairs belonging to the uniformity region.

despite a strong evidence relying on numerical simulations [3]. A plausible explanation concerns the spurious biases in the circuital block generating the variable x that are avoided in the improved design discussed in the present paper.

A. SYNCHRONIZATION ARCHITECTURE

By operating suitable minor changes, the scheme shown in Fig. 2 is suitable to study synchronization among chaotic systems. For the sake of simplicity, we focus the attention on the synchronization between two chaotic systems.

From a general point of view, we can suppose W as the output of a generic unit and S as the synchronization input for the unit. In the case of a laser, W corresponds to the laser output intensity x. Usually the "population inversion" variable y in a laser is physically inaccessible. As a consequence, it is reasonable to perturb the system via the feedback variable z, so S becomes the reference signal on which the synchronization error is built as $\varepsilon\,(S-W)$, where ε represents the coupling strength.

Let us now consider the bidirectional coupling between two laser units as in Fig. 6 by means of the following synchronization error equations:

$$\varepsilon\,(S_1 - W_1) = \varepsilon\,(x_2 - x_1)\ , \tag{23a}$$
$$\varepsilon\,(S_2 - W_2) = \varepsilon\,(x_1 - x_2)\ , \tag{23b}$$

where x_1 is the laser output intensity of the unit of interest and x_2 is the laser output intensity provided by the other unit.

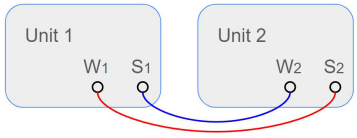

FIGURE 6. Coupling scheme for synchronization between two laser units. W_1 and W_2 are the output of the units, S_1 and S_2 are synchronization input.

Equations (23) represent the perturbation to be added as linear term to the feedback equation (1c). The dynamic behavior of two bidirectional coupled laser system becomes:

$$\frac{dz_1}{dt} = -\beta\ [z_1 - B_0 + B_1 x + \varepsilon(x_2 - x_1)]\ , \tag{24a}$$
$$\frac{dz_2}{dt} = -\beta\ [z_2 - B_0 + B_1 x + \varepsilon(x_1 - x_2)]\ . \tag{24b}$$

For the sake of simplicity, the equations for the laser units (i.e. laser intensity x_1 and x_2, and population inversion y_1 and y_2) are not reported in Eqs. (24).

B. CIRCUIT DESCRIPTION

The coupling dynamics can be implemented in the electrical scheme shown in Fig. 7: The functional block Z, shown in Fig. 7a contains an additional summing node in which the synchronization error is applied. The circuital implementation is shown in Fig. 7b, where the difference term in Eqs.(23) is evaluated by using an additional op-amp AD820 in differential configuration: the signal x is connected to the inverting input and corresponds to the signal x_1; the signal s is connected to the noninverting input and corresponds to the signal x_2. Considering the condition

$$\frac{R_{11}}{R_{12}} = \frac{R_{14}}{R_{13}} \tag{25}$$

the differential output signal is given by

$$\hat{Z} = \frac{R_{11}}{R_{12}}\,(S-W) = \frac{R_{11}}{R_{12}}\,(x_2 - x_1) \tag{26}$$

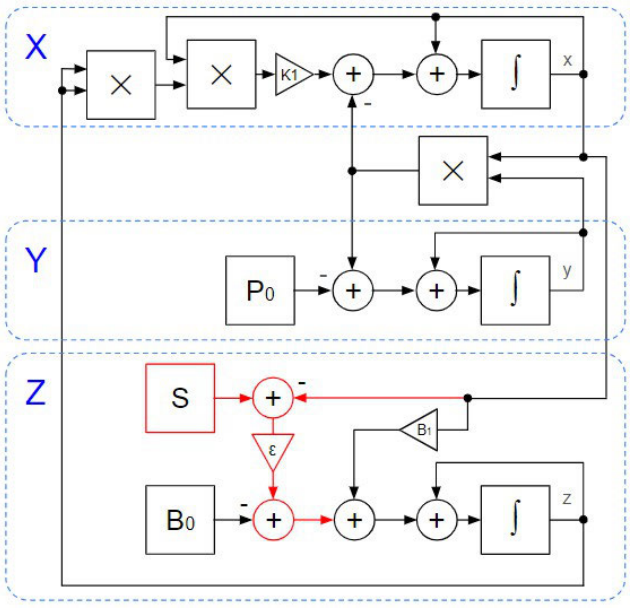

(a)

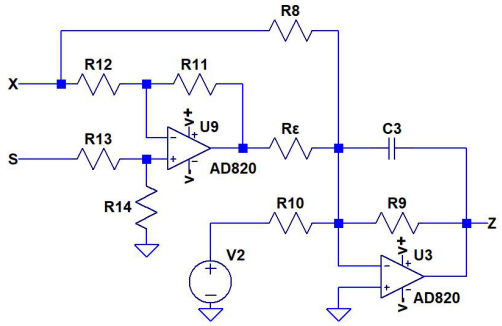

(b)

FIGURE 7. **(a) Design block for synchronization; changes with respect to the single oscillator implementation are highlighted in red. (b) Circuital implementation (block Z).**

By setting

$$R_{11} = R_{12} = R_{13} = R_{14} = 10\,\mathrm{k\Omega} \tag{27}$$

the gain of the differential stage is unitary. It follows

$$\hat{Z} = (x_2 - x_1)\,. \tag{28}$$

The resistor R_ε allows to adjust the coupling strength as

$$\varepsilon = \frac{R_9}{R_\varepsilon}\,. \tag{29}$$

According to Eqs. (24), (29), the system of equations for the bidirectional coupling implementation becomes:

$$-\frac{s}{(R_9C_3)}\,\tilde{z_1} = \tilde{z_1} + \frac{R_9}{R_{10}}\,V_2 + \frac{R_9}{R_8}\,\tilde{x_1} + \frac{R_9}{R_\varepsilon}(\tilde{x_2} - \tilde{x_1}), \tag{30a}$$

$$-\frac{s}{(R_9C_3)}\,\tilde{z_2} = \tilde{z_2} + \frac{R_9}{R_{10}}\,V_2 + \frac{R_9}{R_8}\,\tilde{x_2} + \frac{R_9}{R_\varepsilon}(\tilde{x_1} - \tilde{x_2}). \tag{30b}$$

C. SIMULATION

The fixed and tunable parameter values used in Sec. III-A for the numerical integration and in Sec. III-B for the Spice simulation are also used for synchronization analysis.

The numerical integration analysis was carried out with the following settings of ε

$$\varepsilon \begin{cases} 0 \\ 0.128 \\ 0.168 \end{cases} \quad \text{for SC,} \qquad \varepsilon \begin{cases} 0 \\ 0.128 \\ 0.168 \end{cases} \quad \text{for HC.} \tag{31}$$

The Spice simulation analysis was performed with the following settings of R_ε:

$$R_\varepsilon \begin{cases} 1\,\mathrm{M\Omega} \Rightarrow \varepsilon = 0.001 \\ 10\,\mathrm{k\Omega} \Rightarrow \varepsilon = 0.1 \\ 1\,\mathrm{k\Omega} \Rightarrow \varepsilon = 1 \end{cases} \quad \text{for SC,} \qquad R_\varepsilon \begin{cases} 1\,\mathrm{M\Omega} \Rightarrow \varepsilon = 0.001 \\ 10\,\mathrm{k\Omega} \Rightarrow \varepsilon = 0.1 \\ 1\,\mathrm{k\Omega} \Rightarrow \varepsilon = 1 \end{cases} \quad \text{for HC.} \tag{32}$$

where $R_\varepsilon = 1\,\mathrm{M\Omega}$ is the minimum resistance value that ensures the "no coupling" condition.

Numerical integration has limited resources for coupling system analysis with elevate coupling strength whenever $\varepsilon > 0.2$. Conversely, the electronic simulation allows to test the synchronised system with larger values of correspondent ε by decreasing the resistor R_ε.

The comparison between numerical integration and Spice simulation is displayed in Fig. 8.

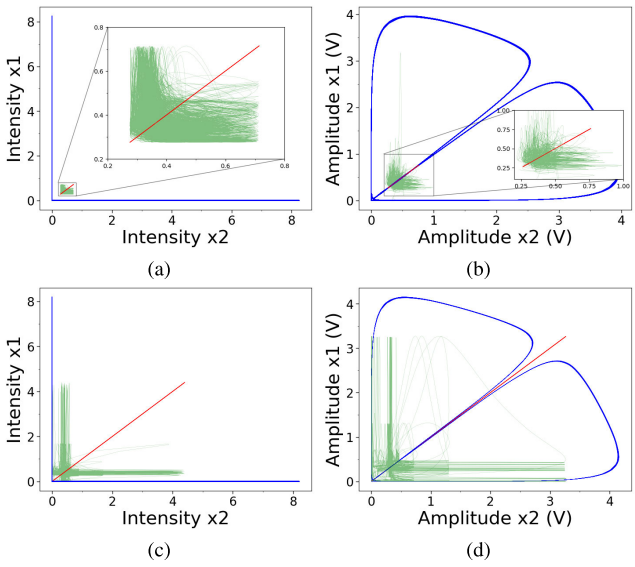

FIGURE 8. **Synchronization of chaos as a function of coupling strength ε. Numerical integration (left panels): (a) synchronization of SC in phase space x_1-x_2; (c) synchronization of HC in phase space x_1-x_2. Spice simulation (right panels): (b) synchronization of SC in phase space x_1-x_2; (d) synchronization of HC in phase space x_1-x_2.**

Figures 8a and 8c show synchronization results (numerical integration) in SC and HC regimes for the three chosen coupling strength values: green color refers to $\varepsilon = 0$

(no coupling); red color to $\varepsilon = 0.128$ (full synchronization); blue color refers to $\varepsilon = 0.168$ (periodic synchronization).

Figures 8b and 8d show synchronization results obtained via Spice simulation in both SC and HC regimes for the three chosen R_ε corresponding to coupling strength values: green color refers to $R_\varepsilon = 1\,\text{M}\Omega$ (no coupling); red color to $R_\varepsilon = 10\,\text{k}\Omega$ (full synchronization); blue color to $R_\varepsilon = 1\,\text{k}\Omega$ (periodic synchronization).

As the coupling strength ε increases, in both SC and HC regimes, the full synchronization of chaos is suddenly transformed in a new periodic synchronization regime (anti-phase synchronization) characterised by high laser intensity amplitudes x_1 and x_2, as shown in Fig. 9.

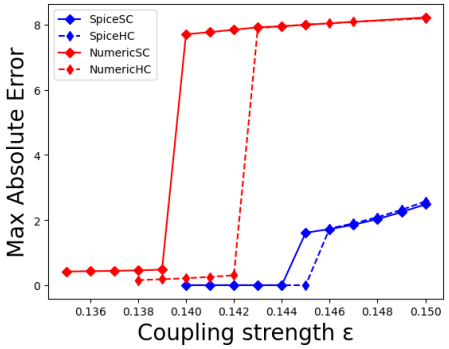

FIGURE 9. Maximum error as a function of the coupling strength ε at the transition from full synchronization to explosive periodic synchronization.

This transition is an evidence of explosive synchronization as investigated by Boccaletti et al. [29].

V. CONCLUSION

The circuital implementation of the minimal universal laser model has been improved by simplifying the topology and removing the saturation effects of electronic devices. Because simulations with two different approaches return equivalent results, the circuital scheme is mature for new network implementations. In this framework, a bidirectional coupling scheme for studying the synchronization in two different chaotic regimes is proposed. In both cases, the full synchronization evolves toward an explosive synchronization regime, which is relevant in brain activity, associated with the onset of anesthesia-induced unconsciousness [30], and in power grid networks [31].

REFERENCES

[1] R. Meucci, S. Euzzor, F. Tito Arecchi, and J.-M. Ginoux, "Minimal universal model for chaos in laser with feedback," *Int. J. Bifurcation Chaos*, vol. 31, no. 4, Mar. 2021, Art. no. 2130013.

[2] L. Ricci, A. Perinelli, M. Castelluzzo, S. Euzzor, and R. Meucci, "Experimental evidence of chaos generated by a minimal universal oscillator model," *Int. J. Bifurcation Chaos*, vol. 31, no. 12, Sep. 2021, Art. no. 2150205.

[3] M. Castelluzzo, M. Cescato, L. Ricci, R. Meucci, and A. Perinelli, "Experimental implementation of a laser model with cavity loss modulation," in *Proc. IEEE Workshop Complex. Eng. (COMPENG)*, Jul. 2022, pp. 1–5.

[4] F. T. Arecchi, W. Gadomski, and R. Meucci, "Generation of chaotic dynamics by feedback on a laser," *Phys. Rev. A, Gen. Phys.*, vol. 34, no. 2, pp. 1617–1620, Aug. 1986.

[5] F. T. Arecchi, "Chaotic neuron dynamics, synchronization and feature binding," *Phys. A, Stat. Mech. Appl.*, vol. 338, nos. 1–2, pp. 218–237, Jul. 2004.

[6] J. A. S. Kelso and A. Fuchs, "Self-organizing dynamics of the human brain: Critical instabilities and Šil'nikov chaos," *Chaos, Interdiscipl. J. Nonlinear Sci.*, vol. 5, no. 1, pp. 64–69, Mar. 1995.

[7] B. Seifert, D. Adamski, and C. Uhl, "Analytic quantification of Shilnikov chaos in epileptic EEG data," *Frontiers Appl. Math. Statist.*, vol. 4, p. 57, Nov. 2018.

[8] B. Shi, C. Luo, J. G. Flor Flores, G. Lo, D.-L. Kwong, J. Wu, and C. W. Wong, "Gbps physical random bit generation based on the mesoscopic chaos of a silicon photonics crystal microcavity," *Opt. Exp.*, vol. 28, no. 24, p. 36685, Nov. 2020.

[9] R. Guo, M. Li, X. Liu, and Z. Wei, "Research on space laser hybrid chaotic shift keying secure communication system," in *Proc. Int. Conf. Wireless Commun. Smart Grid (ICWCSG)*, Jun. 2020, pp. 14–17.

[10] X. Liu, R. Guo, M. Li, and Z. Wei, "Research on image encryption in secure communication system of space laser chaos keying," in *Proc. Int. Conf. Wireless Commun. Smart Grid (ICWCSG)*, Jun. 2020, pp. 10–13.

[11] E. Allaria, F. T. Arecchi, A. Di Garbo, and R. Meucci, "Synchronization of homoclinic chaos," *Phys. Rev. Lett.*, vol. 86, no. 5, pp. 791–794, Jan. 2001.

[12] G. Benettin, L. Galgani, A. Giorgilli, and J.-M. Strelcyn, "Lyapunov characteristic exponents for smooth dynamical systems and for Hamiltonian systems; A method for computing all of them. Part 1: Theory," *Meccanica*, vol. 15, no. 1, pp. 9–20, Mar. 1980.

[13] G. Benettin, L. Galgani, A. Giorgilli, and J.-M. Strelcyn, "Lyapunov characteristic exponents for smooth dynamical systems and for Hamiltonian systems; a method for computing all of them. Part 2: Numerical application," *Meccanica*, vol. 15, no. 1, pp. 21–30, Mar. 1980.

[14] A. Perinelli and L. Ricci, "Chasing chaos by improved identification of suitable embedding dimensions and lags," *Chaos, Interdiscipl. J. Nonlinear Sci.*, vol. 30, no. 12, Dec. 2020, Art. no. 123104.

[15] A. Perinelli and L. Ricci, "Identification of suitable embedding dimensions and lags for time series generated by chaotic, finite-dimensional systems," *Phys. Rev. E, Stat. Phys. Plasmas Fluids Relat. Interdiscip. Top.*, vol. 98, no. 5, Nov. 2018, Art. no. 052226.

[16] J. Gao and Z. Zheng, "Local exponential divergence plot and optimal embedding of a chaotic time series," *Phys. Lett. A*, vol. 181, no. 2, pp. 153–158, Oct. 1993.

[17] M. Franchi and L. Ricci, "Statistical properties of the maximum Lyapunov exponent calculated via the divergence rate method," *Phys. Rev. E, Stat. Phys. Plasmas Fluids Relat. Interdiscip. Top.*, vol. 90, no. 6, Dec. 2014, Art. no. 062920.

[18] L. Ricci, A. Perinelli, and M. Franchi, "Asymptotic behavior of the time-dependent divergence exponent," *Phys. Rev. E, Stat. Phys. Plasmas Fluids Relat. Interdiscip. Top.*, vol. 101, no. 4, Apr. 2020, Art. no. 042211.

[19] L. Pecora and T. Carroll, "Synchronization in chaotic systems," *Phys. Rev. Lett.*, vol. 64, no. 8, pp. 821–824, 1990.

[20] S. Boccaletti, J. Kurths, G. Osipov, D. L. Valladares, and C. S. Zhou, "The synchronization of chaotic systems," *Phys. Rep.*, vol. 366, nos. 1–2, pp. 1–101, 2002.

[21] U. E. Kocamaz, S. Çiçek, and Y. Uyaroğlu, "Secure communication with chaos and electronic circuit design using passivity-based synchronization," *J. Circuits, Syst. Comput.*, vol. 27, no. 4, Apr. 2018, Art. no. 1850057.

[22] A. Khitun, M. Bao, J.-Y. Lee, K. L. Wang, D. W. Lee, S. X. Wang, and I. V. Roshchin, "Inductively coupled circuits with spin wave bus for information processing," *J. Nanoelectronics Optoelectronics*, vol. 3, no. 1, pp. 24–34, Mar. 2008.

[23] S. Boccaletti, A. N. Pisarchik, C. I. del Genio, and A. Amann, *Synchronization: From Coupled Systems to Complex Networks*. Cambridge, U.K.: Cambridge Univ. Press, 2018.

[24] A. Uchida, M. Shinozuka, T. Ogawa, and F. Kannari, "Experiments on chaos synchronization in two separate microchip lasers," *Opt. Lett.*, vol. 24, no. 13, p. 890, 1999.

[25] T. Sugawara, M. Tachikawa, T. Tsukamoto, and T. Shimizu, "Observation of synchronization in laser chaos," *Phys. Rev. Lett.*, vol. 72, no. 22, pp. 3502–3505, May 1994.

[26] S. Sivaprakasam and K. A. Shore, "Demonstration of optical synchronization of chaotic external-cavity laser diodes," *Opt. Lett.*, vol. 24, no. 7, p. 466, 1999.

[27] S. Sivaprakasam and K. A. Shore, "Cascaded synchronization of external-cavity laser diodes," *Opt. Lett.*, vol. 26, no. 5, p. 253, 2001.
[28] M. Mehrabbeik, S. Jafari, R. Meucci, and M. Perc, "Synchronization and multistability in a network of diffusively coupled laser models," *Commun. Nonlinear Sci. Numer. Simul.*, vol. 125, Oct. 2023, Art. no. 107380.
[29] S. Boccaletti, J. A. Almendral, S. Guan, I. Leyva, Z. Liu, I. Sendiña-Nadal, Z. Wang, and Y. Zou, "Explosive transitions in complex networks' structure and dynamics: Percolation and synchronization," *Phys. Rep.*, vol. 660, pp. 1–94, Nov. 2016.
[30] M. Kim, G. A. Mashour, S.-B. Moraes, G. Vanini, V. Tarnal, E. Janke, A. G. Hudetz, and U. Lee, "Functional and topological conditions for explosive synchronization develop in human brain networks with the onset of anesthetic-induced unconsciousness," *Frontiers Comput. Neurosci.*, vol. 10, p. 1, Jan. 2016.
[31] A. E. Motter, S. A. Myers, M. Anghel, and T. Nishikawa, "Spontaneous synchrony in power-grid networks," *Nature Phys.*, vol. 9, no. 3, pp. 191–197, Mar. 2013.

ROBERTO CONCAS received the B.Sc. and M.Sc. degrees in electronics engineering from the University of Cagliari, Italy.

He has been working with Istituto Nazionale di Ricerca Metrologica (INRiM), since 2018. He is currently a member with the Electronic Workshop, European Laboratory for Non-Linear Spectroscopy (LENS). With more than 15 years experience in electronic design, hardware and firmware development, he has been collaborating in different fields such as domotics, the IoT, materials engineering, biotechnology, quantum technology, and spectroscopy.

ALESSIO MONTORI has been working with the National Institute of Optics (CNR), since 2012 and he also has been collaborating with the Electronic Workshop, European Laboratory for Non-Linear Spectroscopy (LENS). Since 2022, he has been the role of the CTO in ppqSense S.r.l., a company that commercializes the first radiocarbon measurement system based on a CNR-patented spectroscopic technique. He is currently an Electronics Technician with a specialization in optoelectronics. He has more than 20 years of experience in designing ultra-low noise electronics for precision spectroscopy applications.

EUGENIO PUGLIESE received the degree in physics and the Ph.D. degree, working on topics in nonlinear dynamics and complex systems. His research activity is currently focused on the development of imaging techniques for various applications. He is the coauthor of numerous publications both in the field of the dynamics in classical and quantum systems and in the field of optics and digital holography.

ALESSIO PERINELLI received the M.S. and Ph.D. degrees in physics from the University of Trento, in 2017 and 2020, respectively. He is currently a Researcher with the Department of Physics, University of Trento. His research interests include the investigation of nonlinear and chaotic systems, the development of nonlinear time series analysis methods, the application of nonlinear methods to signals generated by complex systems in different fields, and from neuroscience to geoscience.

LEONARDO RICCI (Member, IEEE) received the M.S. degree in physics from the University of Pisa, Pisa, Italy, in 1990, and the Ph.D. degree in physics from the Ludwig-Maximilian University, Munich, Germany, in 1994. From 1990 to 1994, he was with T. W. Sch's Group, Munich. In 1995, he moved to the Department of Physics, University of Trento, Trento, Italy, where is currently an Associate Professor. His research interests include complex systems dynamics, entropy (information theory), and the development of nonlinear techniques for time series analysis.

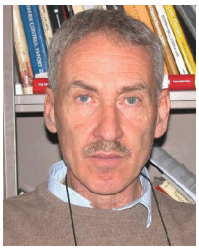

RICCARDO MEUCCI (Senior Member, IEEE) was born in Scandicci, Florence, Italy, in 1956. He received the Ph.D. degree in physics and the Ph.D. degree (Hons.) specialization in optics from the University of Florence, Italy, in 1982 and 1987, respectively.

Since 1987, he has been with the National Institute of Optics, Florence, where he holds the position of the Research Director. He is currently a Contract Professor of physical optics and mathematical methods for optics with the University of Florence. His research interests include nonlinear dynamics, chaos, control of chaos, synchronization, and infrared digital holography. From 1984 to 1987, he was a Research Fellow with Istituto di Cibernetica, National Research Council (CNR), Italy.

Open Access funding provided by 'Istituto Nazionale di Ricerca Metrologica - INRiM' within the CRUI CARE Agreement